ADVANCED ENERGY MATERIALS

Supporting Information

for *Adv. Energy Mater.,* DOI: 10.1002/aenm.201801289

In Situ “Chainmail Catalyst” Assembly in Low-Tortuosity, Hierarchical Carbon Frameworks for Efficient and Stable Hydrogen Generation

*Yiju Li, Tingting Gao, Yonggang Yao, Zhenyu Liu, Yudi Kuang, Chaoji Chen, Jianwei Song, Shaomao Xu, Emily M. Hitz, Boyang Liu, Rohit J. Jacob, Michael R. Zachariah, Guofeng Wang, and Liangbing Hu**

SUPPLEMENTARY INFORMATION

In-Situ "Chainmail Catalyst" Assembly in Low-Tortuosity, Hierarchical Carbon Frameworks for Efficient and Stable Hydrogen Generation

Yiju Li[1 a], Tingting Gao[1 a], Yonggang Yao[1 a], Zhenyu Liu[3], Yudi Kuang[1], Chaoji Chen[1], Jianwei Song[1], Shaomao Xu[1], Emily M. Hitz[1], Boyang Liu[1], Rohit Jiji Jacob[2], Michael R. Zachariah[2], Guofeng Wang[3], Liangbing Hu[1, *]

[1]*Department of Materials Science and Engineering, University of Maryland, College Park, Maryland, 20742, USA*
[2]*Department of Chemical Engineering and Chemistry, University of Maryland, College Park, Maryland, 20742, USA*
[3]*Department of Mechanical Engineering and Materials Science, University of Pittsburgh, Pennsylvania, 15261, USA*

[a] These authors contributed equally.
[*] Email: binghu@umd.edu

Table of Contents

Supplementary Method S3. DFT calculation of Free Energy of Hydrogen Adsorption
Table S2. Summary of hydrogen chemisorption energy, zero-point energy correction and free energy of adsorption of various N-doped graphene species.
Figure S13. Differential charge density with respect to the superposition of atomic charge density and electronic density of states of pyrrolic N doped graphene with and without encapsulated Ni_3Fe clusters.
Figure S14. Wettability test of the CW-CNT@N-C-NiFe electrode.
Figure S15. C_{dl} calculation of the CW-CNT and CNT.
Table S3. Summary of HER activities of various non-noble metal and metal alloy electrocatalysts in acidic electrolyte.

Materials and Methods

Preparation of CW Framework

First, the natural wood block was cut perpendicular to the growth direction to obtain the wood slice. The wood slice was pre-treated under 260°C for 6 h and then carbonized under 1,000°C for 6 h in an argon atmosphere. Next, the obtained carbonized wood was cut into pieces (2 cm × 2 cm) for *in-situ* CNT growth.

Preparation of CW-CNT Composite Framework

The CW was first immersed into the nickel nitrate ($Ni(NO_3)_2$) solution (0.05 g mL^{-1}) and ultrasonicated for 5 min. The infiltrated CW was then vertically placed in the middle of a quartz tube furnace, of which the direction of microchannel inside the CW is the same with the air flow. The polyvinylpyrrolidone powders (average molar mass: 40,000) were loaded into a quartz boat and placed in the upstream of the quartz tube. Initially, argon gas flow (99.99%) was maintained over the quartz tube to remove air. The furnace was then heated from room temperature to 900^{o}C for 2 h at a ramp rate of 15^{o}C min^{-1} and cooled down naturally. Finally, the obtained CW-CNT framework was dipped in hydrochloric acid solution and then washed with deionized water.

Preparation of CW-CNT@N-C-NiFe Electrode

The as-prepared CW-CNT framework was dipped into a solution containing 6.0 g L^{-1} nickel chloride ($NiCl_2$), 3.0 g L^{-1} ferrous chloride ($FeCl_2$), 10 g L^{-1} polyvinylpyrrolidone and 10 g L^{-1} urea ($CO(NH_2)_2$). After dry at 60^oC under vacuum, the CW-CNT framework was cut into strip-like structure (2 cm × 2 mm) and mounted on the home-made concave glass shelf. Direct current pulse (current: 1 A; time: 45 ms) was then applied on the strip-like CW-CNT framework using the Keithley power supply in a vacuum chamber. After cooling down to ambient temperature, the sample was peeled from the glass shelf and washed using deionized water. The mass loading of the N-C-NiFe nanoparticles is about 0.15 mg cm^{-2}. As a comparison, the electrode treated with conventional pyrolysis in tube furnace (TF) under argon atmosphere (temperature: 1,000^oC; time: 1 h; temperature ramp rate: 10^oC min^{-1}) is denoted as CW-CNT@C-NiFe-TF. For the two methods (heat shock and the conventional pyrolysis in tube furnace), the amounts of metal salts and carbon sources are the same.

Characterization Methods

SEM images were acquired using a Hitachi SU-70 field emission microscope equipped with an energy dispersive spectrometer. TEM and HRTEM were conducted on a field emission TEM/STEM microscope (JEM 2100). The XRD patterns were obtained using a Bruker C2 Discover X-Ray Powder Diffractometer. The composition of the NiFe bimetallic alloy nanoparticles was detected by ICP-MS (Thermo XSeries II). The surface chemical composition was attained using XPS (Thermo ESCALAB 250).

Electrochemical Measurements

The electrocatalytic performance measurement of HER was conducted in a standard three-electrode setup using a computerized electrochemistry workstation (VMP3/Z Bio-Logic) controlled by the EC-lab software. The CW-CNT@N-C-NiFe composite directly acts as the freestanding and binder-free working electrode for HER. A saturated Ag/AgCl electrode is

selected as the reference electrode and a graphite rod is served as the counter electrode. 0.5 M H_2SO_4 solution was used as the electrolyte. LSV was adopted to attain the polarization curves by sweeping the potential within the range from 0 to −0.8 V (*vs.* Ag/AgCl) at a potential scan rate of 5 mV s^{-1}. Accelerated cycling durability measurements were conducted by potential cycling between 0.1 and -0.25 V (*vs.* RHE) at a scan rate of 100 mV s^{-1}. The chronoamperometric curve was obtained with a set overpotential of 185 mV for 480 min. EIS was conducted at various overpotentials with a voltage amplitude of 5 mV in the frequency range of 10 mHz to 100 kHz.

Supplementary Method S1. Temperature and Time Measurement

To accurately obtain the temperature and time of the heated samples during the treatment of rapid heat shock, the device should be able to quickly collect the light emitted from the heated sample. A high-speed spectrometer (Acton SP 500i with a 150 L mm^{-1} grating) with sub-millisecond time resolution was used to detect and collect the emitted light. The generated emission spectra were then sent into the multi anode PMT array (32 channels) equipped with a high-speed and accurate data acquisition system (Vertilon IQSP 580). The system was first calibrated based on a black body heater in the temperature range of 1,200-1,500 K, and the sample rate in the data acquisition system was set at 10 kHz. The time-resolved spectra were obtained over the wavelength range of 440-858 nm (collected from 30 channels in PMT) and fitted based on the Planck's law to calculate the temperature.[1] The Planck function is shown below.

$$I_\lambda(\lambda,T) = \gamma\varepsilon_{gray}\frac{2hc^2}{\lambda^5\left[\exp\left(\frac{hc}{\lambda k_B T}\right)-1\right]}$$

where k_B represents the Boltzmann constant, h is the Planck constant, c is the speed of light, T represents the temperature, ε_{gray} is constant gray emissivity (~0.8 for carbon), λ is the wavelength, and γ is the scaling constant between the heated sample and optical fiber.

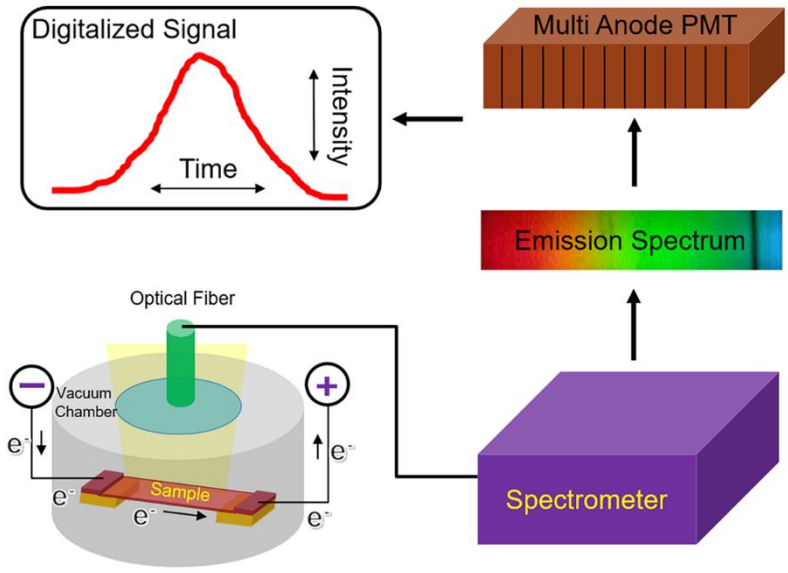

Figure S1. Schematic of the device used for high-speed spectroscopic temperature and time measurement during the heat shock treatment.

Supplementary Method S2. Tortuosity Measurement

In our work, the tortuosity of the samples was measured using the AC impedance as a function of the frequency of excitation. The natural wood and carbonized wood-based samples were sandwiched between two thin porous polypropylene film (thickness: 8 μm) to avoid short circuit. A schematic of the tortuosity measurement device is shown in Figure S2a. Figure S2b shows the Nyquist plots of the samples at open circuit potential with a voltage amplitude of 5 mV. The intercept with the x-axis at high frequency can represent the resistance of the solution in the pores

of the samples (R_S). According to previously reported works,[2,3] the tortuosity (ε) can be calculated based on the following equation:

$$\varepsilon = Rs * A * \varepsilon / (\rho * L)$$

Where Rs is the solution resistance in the pores of the samples, A is the transversal area of the samples (1.26 cm^2), ε denotes the porosity (natural wood: ~64%; CW: ~70%; CW-CNT: ~68%; CW-CNT@N-C-NiFe: ~67%), ρ represents the resistivity of the electrolyte (100 Ω·cm for standard 1 M $LiPF_6$ in EC/DEC), L is the thickness of the samples (1.2 mm). The tortuosity values of the natural wood, CW, CW-CNT and CW-CNT@N-C-NiFe are calculated to be 1.28, 1.15, 1.31 and 1.30, respectively.

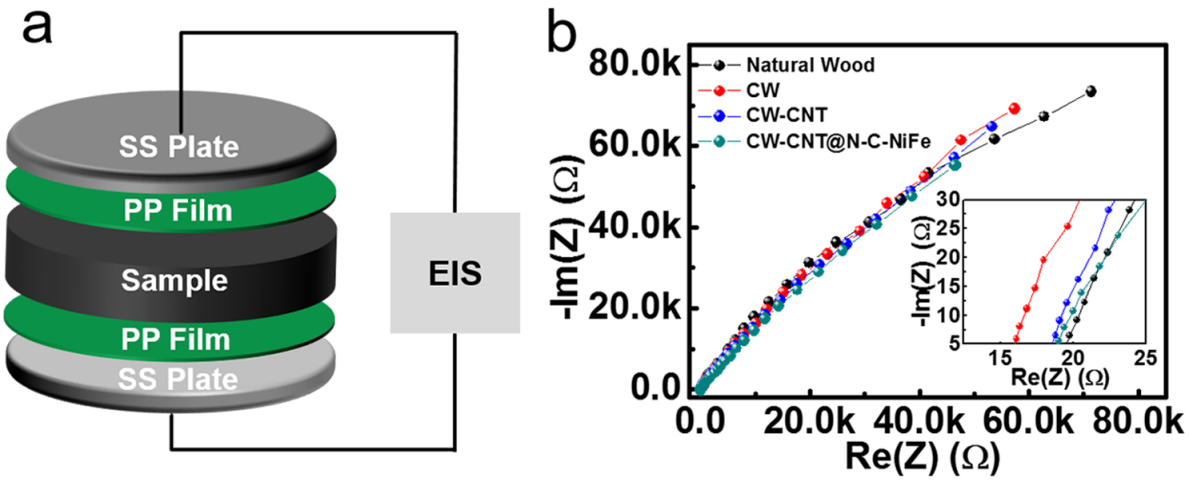

Figure S2. (a) Schematic illustration showing the device used for tortuosity testing. (b) Nyquist curves of the various samples at open circuit potential. Inset in Figure S2b is a zoomed-in view of the Nyquist curves.

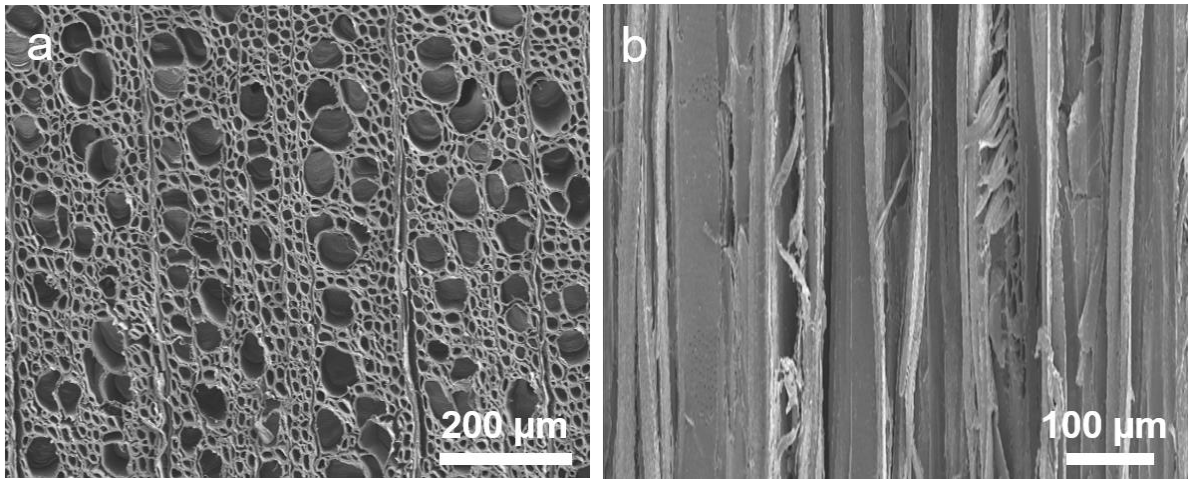

Figure S3. (a) SEM image of the top surface of the natural wood. (b) SEM image of the cross-section of the natural wood, which displays the naturally aligned microchannels.

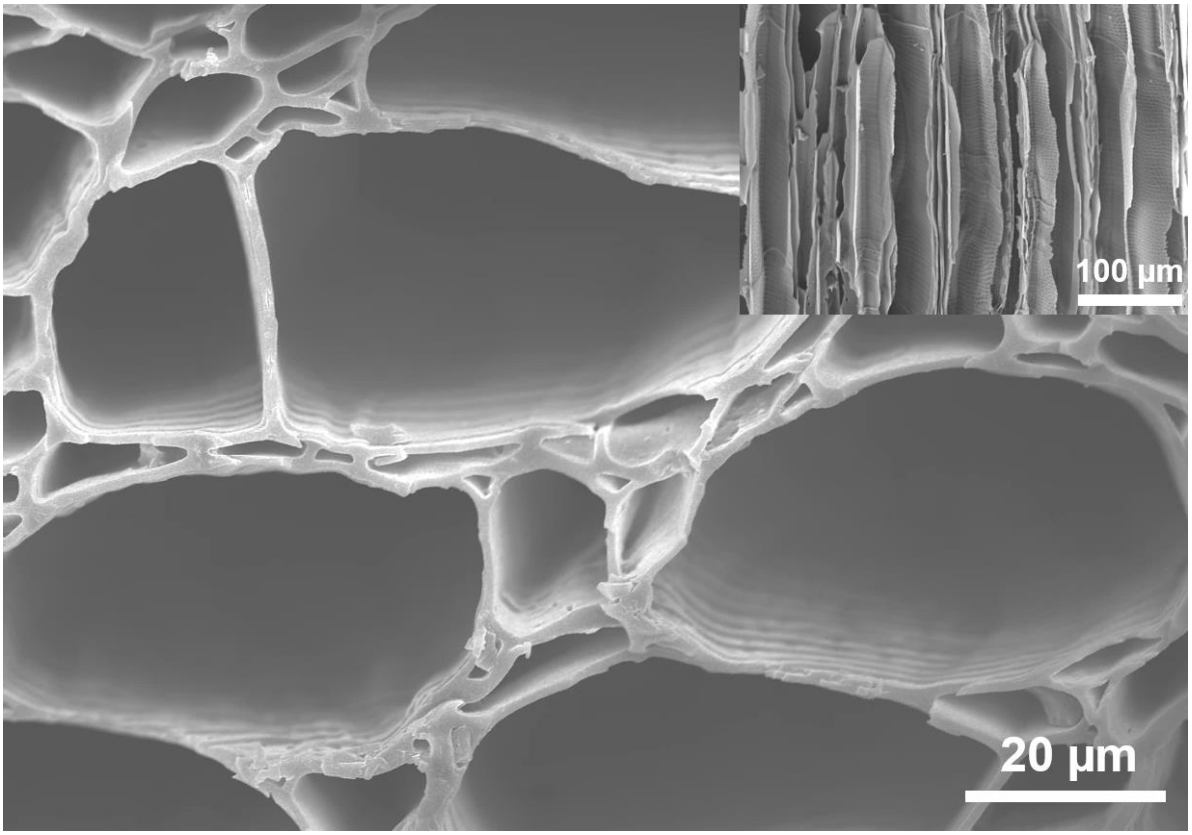

Figure S4. SEM image of the top surface of the carbonized wood. The aligned and open

microchannels are perfectly preserved after carbonization (inset).

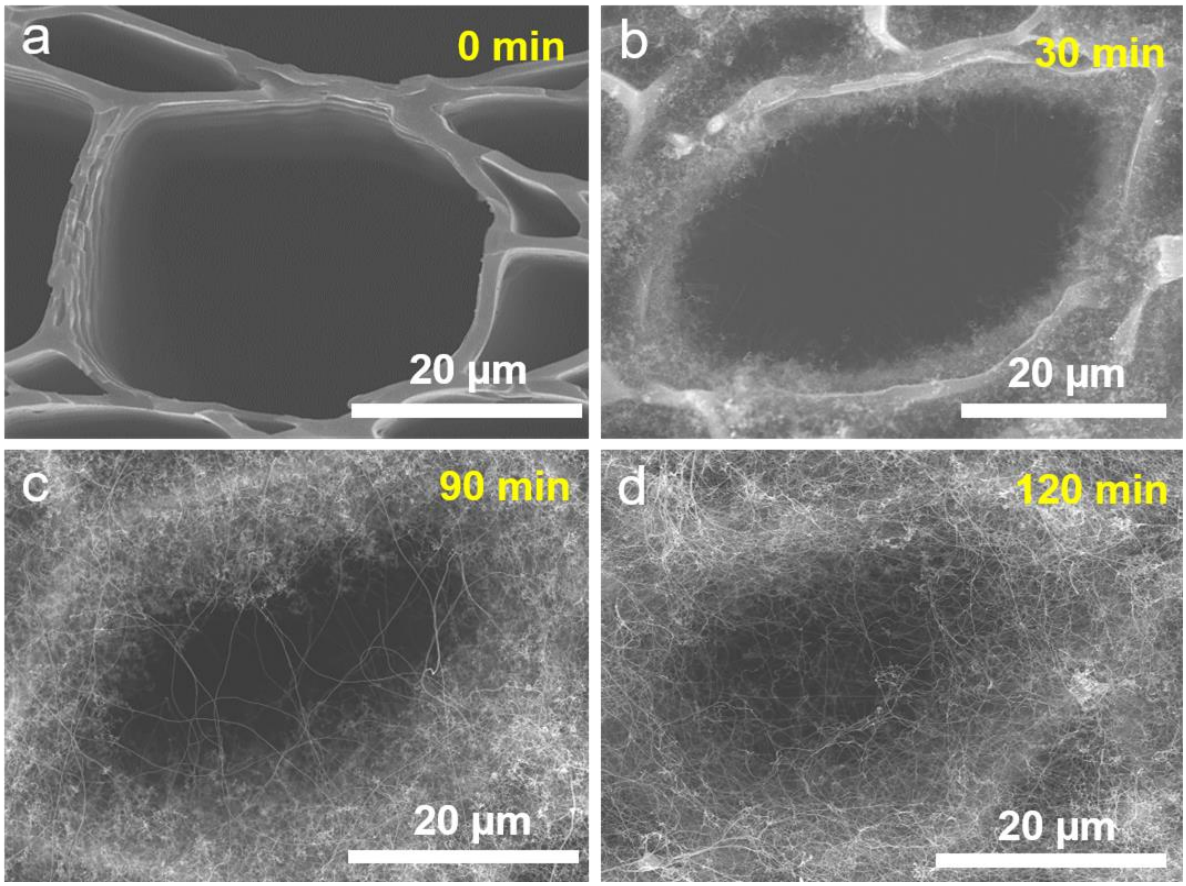

Figure S5. SEM images revealing the process of CNT growth in the carbonized wood framework with different time duration of (a) 0, (b) 30, (c) 90 and (d) 120 min.

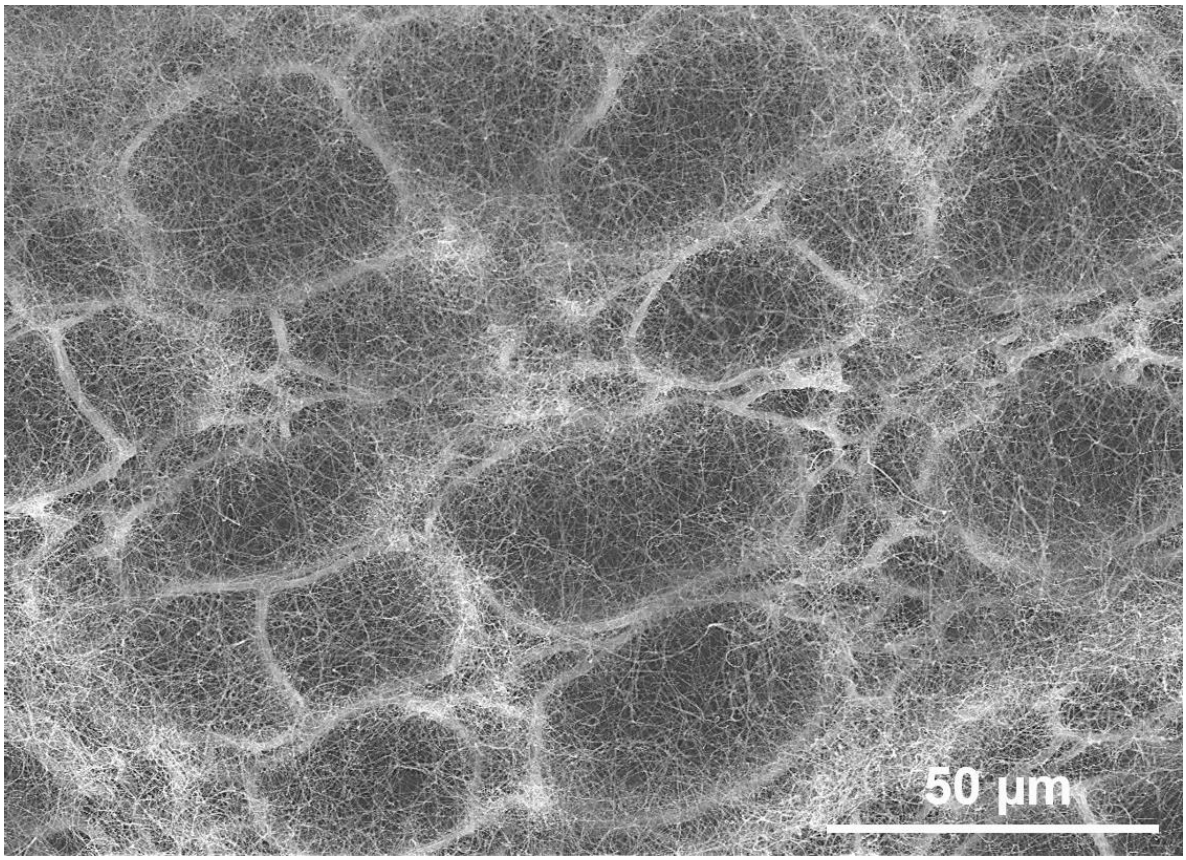

Figure S6. SEM image showing the top surface of the CW-CNT composite. The microchannels are filled with interconnected CNTs.

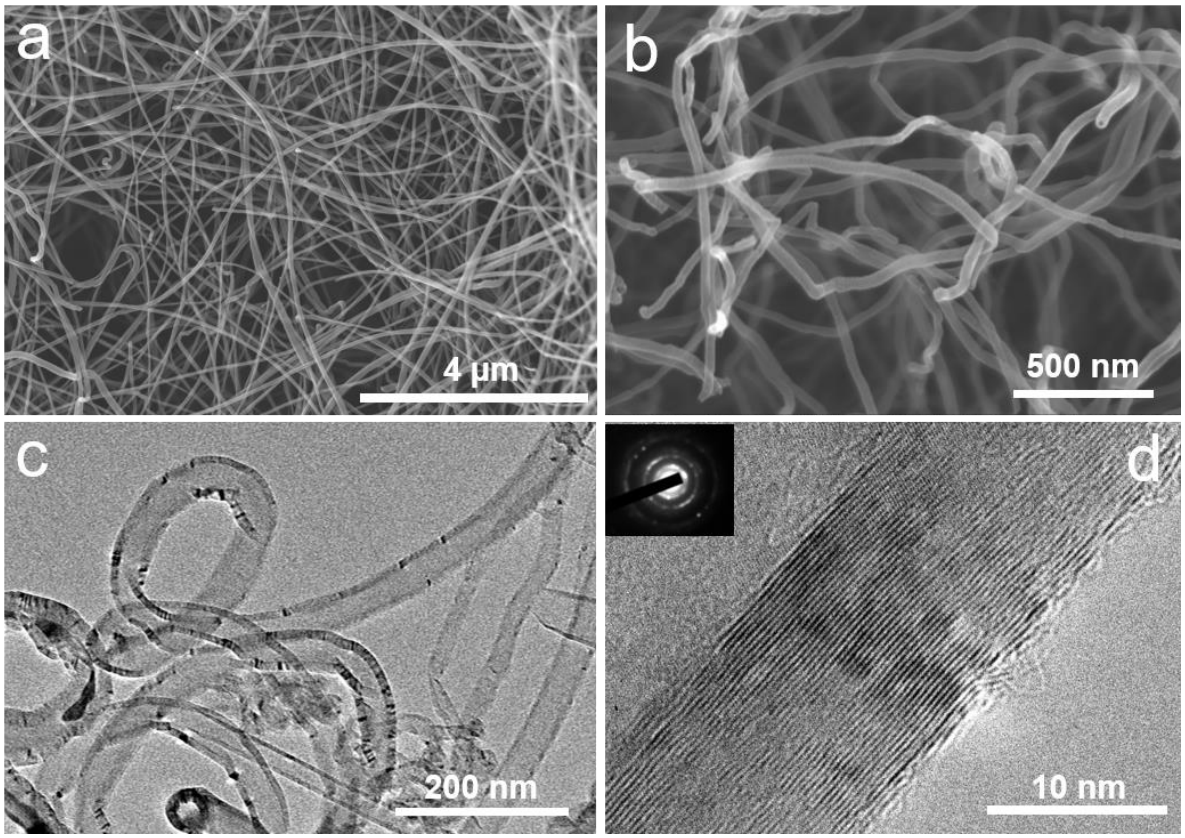

Figure S7. (a, b) SEM images of the CNTs. (c, d) TEM images of the CNTs. Inset in Figure S7d is the SAED pattern of CNT, revealing the favorable crystallization. The wall thickness of the CNT is about 14 nm.

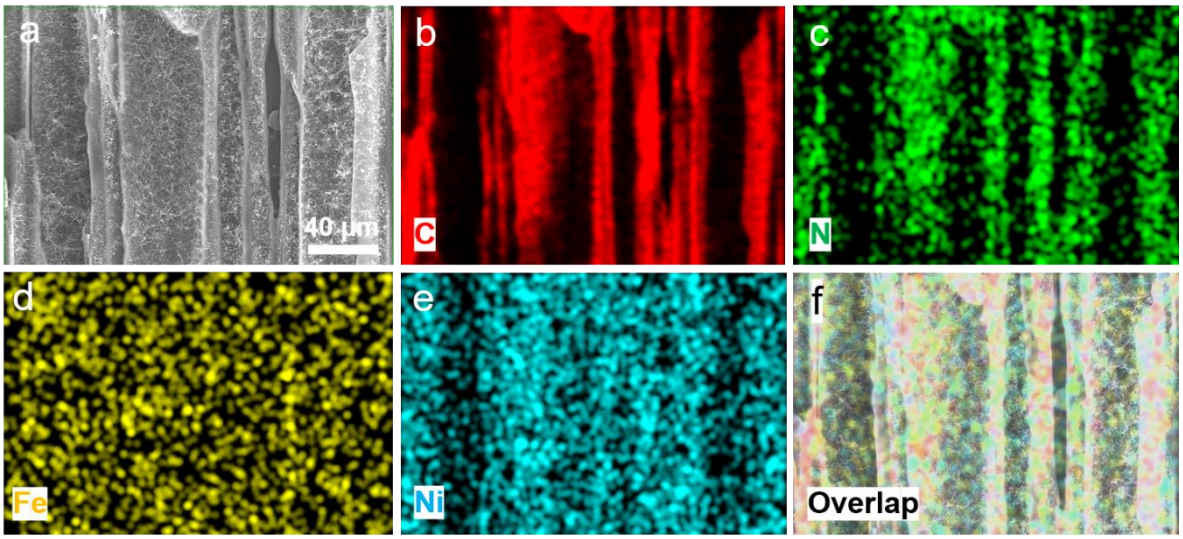

Figure S8. SEM image and elemental mappings (C, N, Fe and Ni) of the cross-section of the CW-CNT@N-C-NiFe composite, indicating the uniform distribution of the N-C-NiFe nanoparticles in the CW-CNT framework.

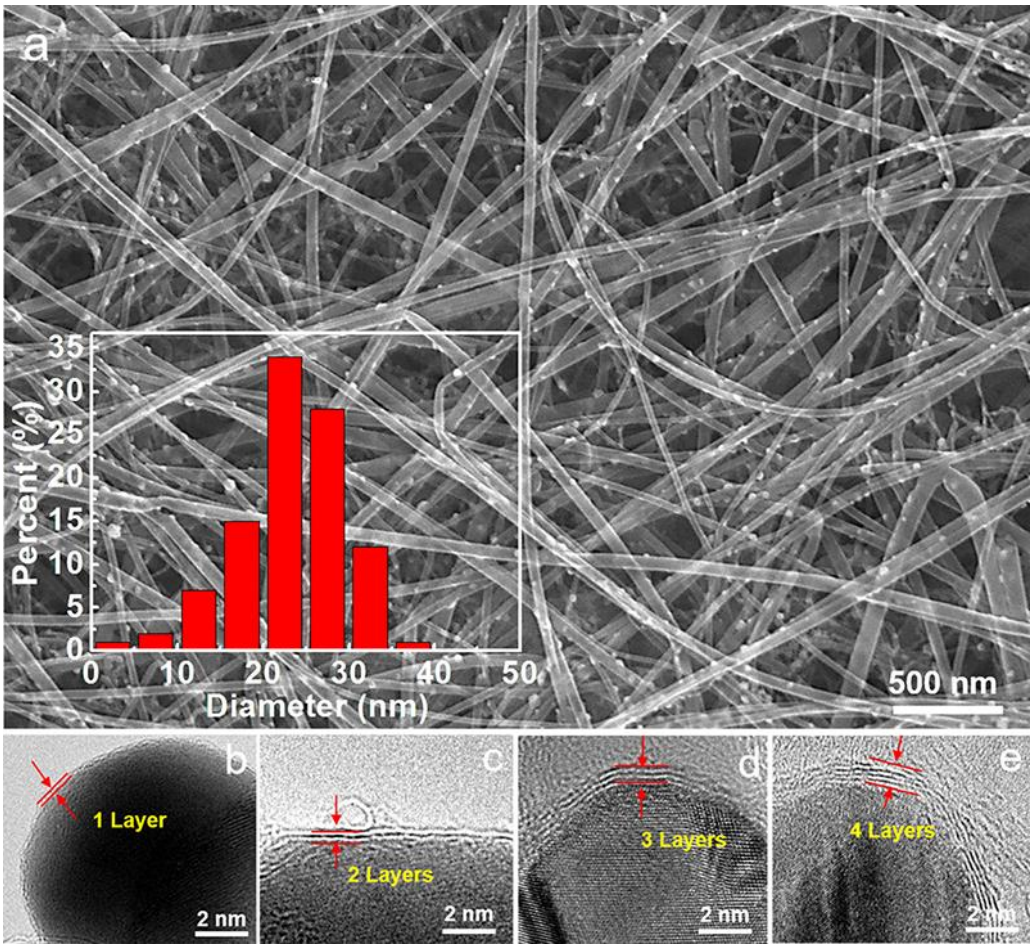

Figure S9. (a) SEM image showing the CNTs loaded with the N-C-NiFe nanoparticles. The N-C-NiFe nanoparticles are uniformly dispersed on the interconnected CNTs network. Inset is the size distribution of the N-C-NiFe nanoparticles. The average diameter of the N-C-NiFe nanoparticles is ~22.5 nm. (b-e) TEM images showing the N-C-NiFe nanoparticles are encapsulated by different layers of graphene.

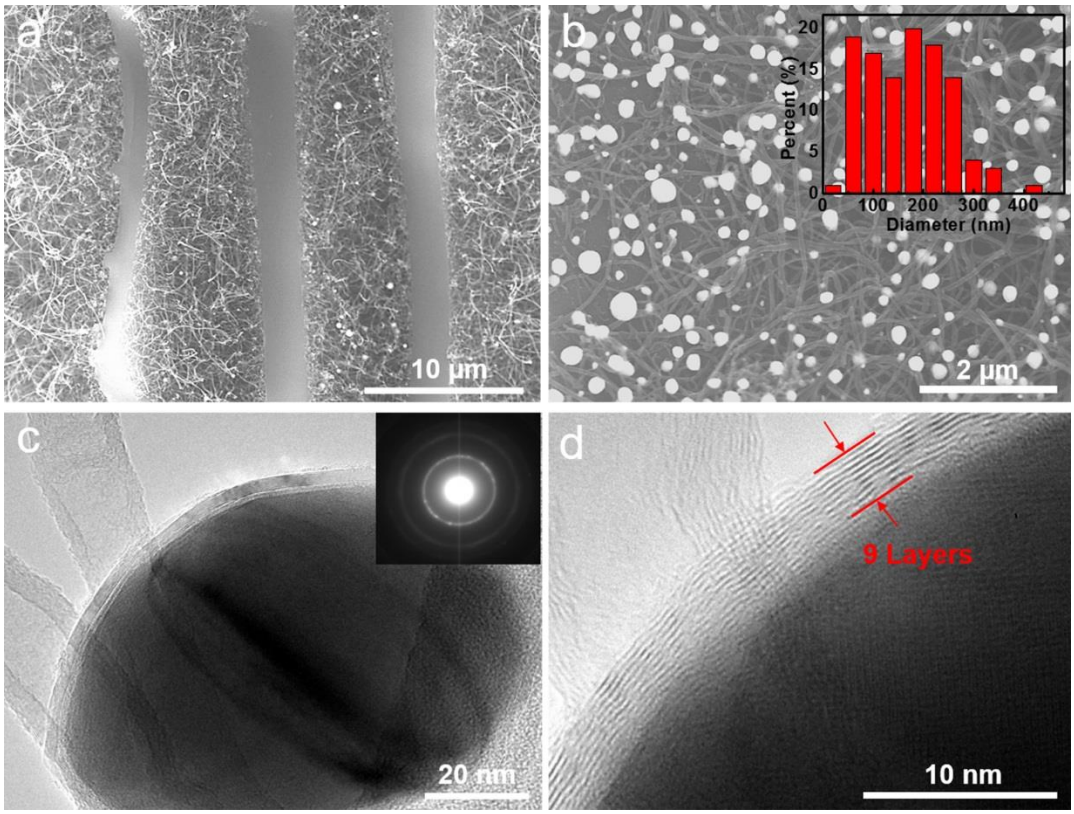

Figure S10. Morphology characterization of the NiFe nanoparticles treated with conventional pyrolysis in tube furnace under argon atmosphere. (a) SEM image of the cross-section of the CW-CNT@C-NiFe-TF composite. (b) SEM image showing the CNT network decorated with NiFe nanoparticles. Inset in Figure S8b showing the size distribution. The size of the NiFe alloy nanoparticles treated with conventional pyrolysis is inhomogeneous and can reach up to ~500 nm, which is 22.2 times larger than that of the N-C-NiFe nanoparticles synthesized by the heat shock method. The large particle size of the C-NiFe-TF could be attributed to the long heating time and slow cooling rate, resulting in the gradual agglomeration of small nanoparticles. (c, d) TEM images of the C-NiFe-TF nanoparticle. The C-NiFe-TF nanoparticle is encapsulated by 9 graphene layers, which is thicker than the layer present on the N-C-NiFe nanoparticles (1-4 layers). Inset in Figure S8c shows the SAED pattern of the C-NiFe-TF nanoparticle.

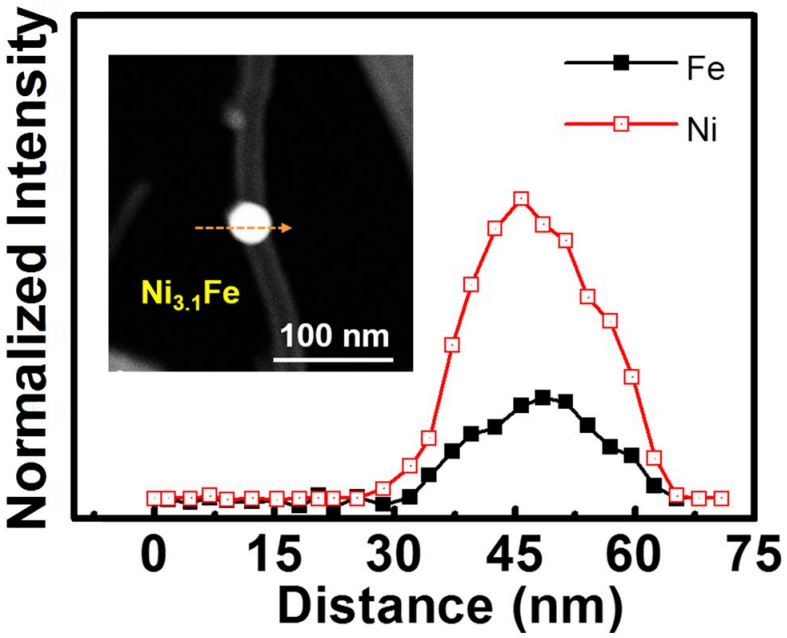

Figure S11. STEM-EELS line scan analysis of the N-C-NiFe nanoparticle. Inset is the HAADF-STEM image of the corresponding N-C-NiFe nanoparticle.

Table S1. Elemental Content of the CW-CNT@N-C-NiFe electrode (excluding Fe and Ni).

Elements	Contents (at%)
C	92.11
O	4.87
N	3.02

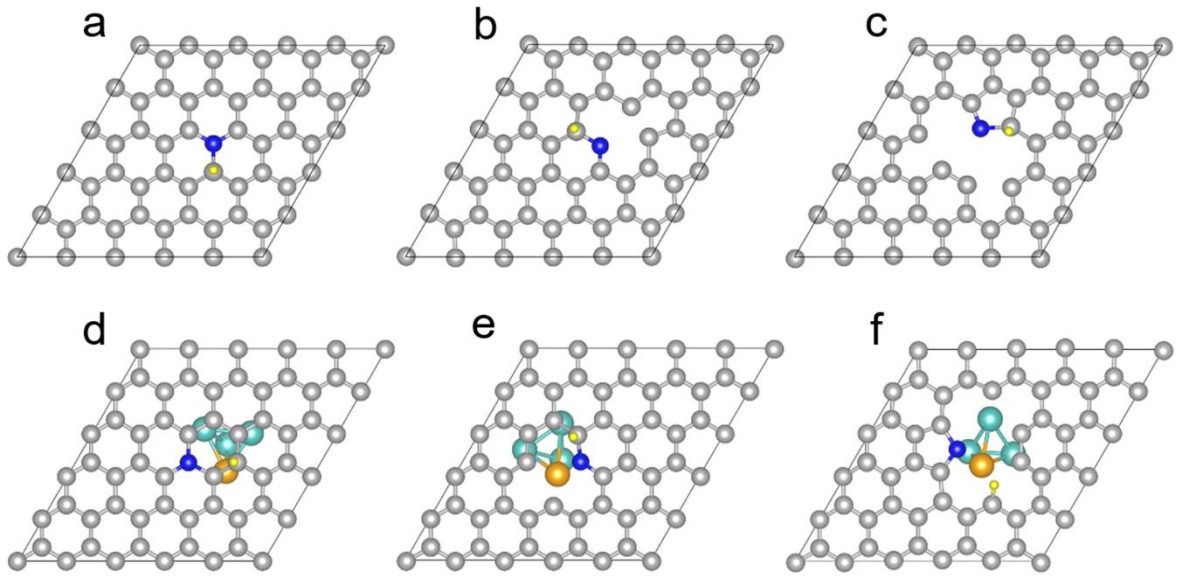

Figure S12. Optimized atomic structure of H* adsorbed on various N-doped graphene species. (a) quaternary N (b) pyridinic N (c) pyrrolic N and (d) Ni_3Fe/quaternary N (e) Ni_3Fe/pyridinic N (f) Ni_3Fe/pyrrolic N. In the figures, the gray, blue, yellow, gold, cyan balls represent C, N, H, Fe and Ni atoms, respectively.

Supplementary Method S3. Calculation of Free Energy of Hydrogen Adsorption

The DFT calculations were performed using the VASP within the formulism of plane wave basis and PAW method.[4,5] The revised Perdew-Burke-Ernzerhof (rPBE) functionals were employed to evaluate the exchange-correlation energy.[6] The kinetic energy cutoff of 400 eV was used for plane wave expansion and the total energy was converged to 10^{-6} eV. The atomic positions were optimized until the Hellman-Feynman force on each ion was below 0.02 eV/Å. A gamma centered k-point mesh of 4×4×1 was used for the Brillouin zone integration. As shown in Figure S12, the structure of N doped graphene active site was modeled with a hexagonal graphene supercell with periodic boundary conditions in all dimensions. A vacuum layer of 14 Å was added above the graphene layer to minimize the interaction between periodic images.

Table S2. Summary of hydrogen chemisorption energy, zero-point energy correction and free energy of adsorption of various N-doped graphene species and Ni_3Fe cluster.

	Quaternary N	Pyridinic N	Pyrrolic N	Ni_3Fe/Quaternary N	Ni_3Fe /Pyridinic N	Ni_3Fe/Pyrrolic N	Ni_3Fe
ΔE_H	0.57	1.42	0.31	0.49	0.86	-0.41	-0.57
ΔE_{ZPE}	0.18	0.16	0.16	0.17	0.17	0.17	0.01
ΔG_{H^*}	**0.95**	**1.78**	**0.67**	**0.87**	**1.24**	**-0.03**	**-0.35**

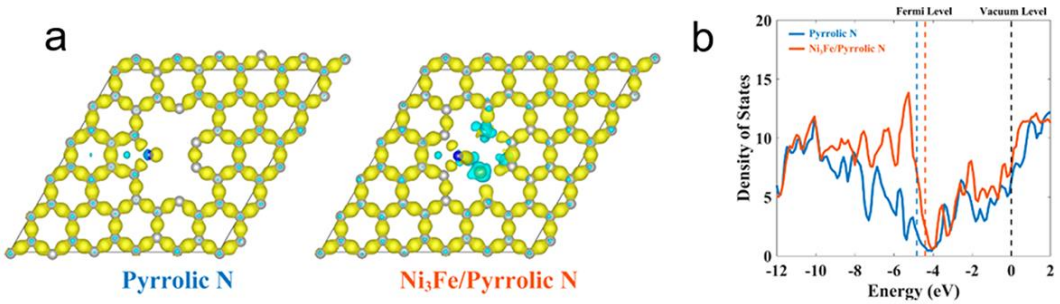

Figure S13. (a) Differential charge density with respect to the superposition of atomic charge density; yellow (blue) regions depict an increase (decrease) in electron density; modeled pyrrolic N doped graphene (left) and modeled pyrrolic N doped graphene with encapsulated Ni_3Fe clusters (right); (b) Electronic density of states of pyrrolic N doped graphene with and without encapsulated Ni_3Fe clusters; the vacuum level is aligned at 0 eV.

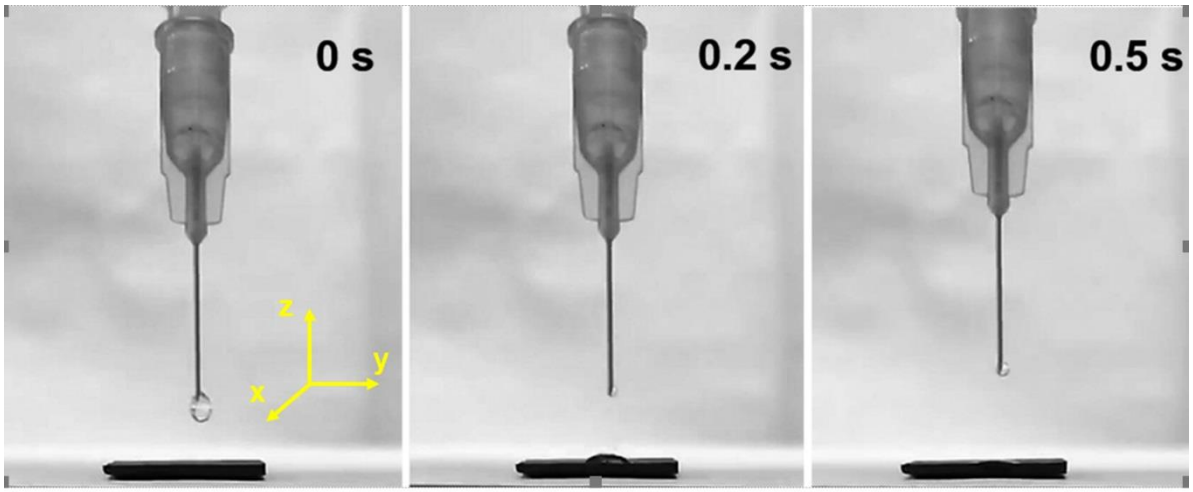

Figure S14. Wettability test of the CW-CNT@N-C-NiFe electrode. The contact angle of ~0^o indicates the excellent solution wettability of the electrode.

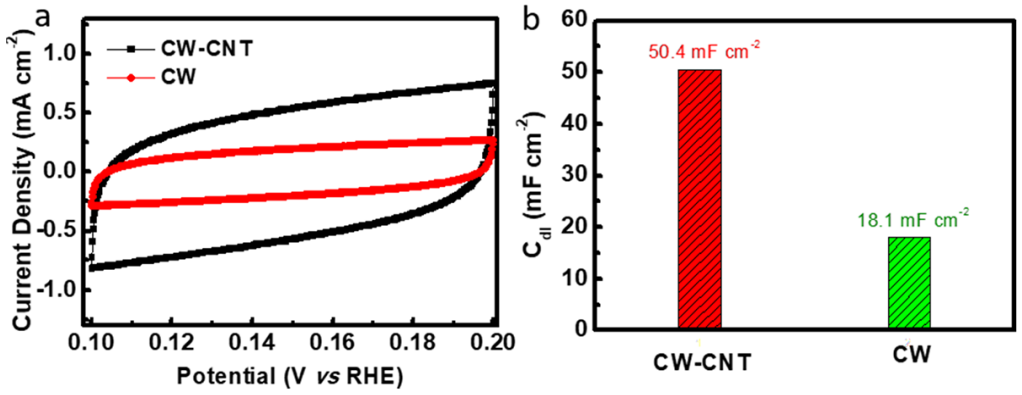

Figure S15. (a) CV curves of the CW-CNT and CNT at a scan rate of 10 mV s^{-1} (0.1−0.2 V *vs* RHE). (b) C_{dl} comparison of the CW-CNT and CNT.

Table S3. Summary of HER activities of various non-noble metal and metal alloy electrocatalysts in acidic electrolyte.

Electrocatalysts	Overpotential at j=10 mA cm^{-2} (mV)	Tafel slope (mV dec^{-1})	Catalyst loading (mg cm^{-2})	Scan rate (mV s^{-1})	Self-standing or not	Ref.
Co@N-doped graphene film	124.6	93.9	N/A	5	Yes	[7]
N-Co@G	265	98	0.285	5	No	[8]
Co@NC/N-doped graphene	190	79.3	0.285	5	No	[9]
Atomic Co/NG	147	82	0.285	2	No	[10]
FeCo@NCNTs-NH	275	74	0.32	2	No	[11]
Co@NCN-800	200	82	0.285	5	No	[12]
NiFe-NGT-800	140	63.4	0.35	2	No	[13]
Ni−Sn@C	360	35	0.1	5	No	[14]
Ni foam	210	100	N/A	5	Yes	[15]
Co@NC-Ti	106	78.2	11.2	5	Yes	[16]
Co@N-C	200	100	4.5	2	No	[17]
Co-NCNT/CC	78	74	3.4	5	Yes	[18]
Co@CN	191	116.3	N/A	5	No	[19]
S-600	262	74	0.285	2	No	[20]
CoNi@NC	224	104	0.32	2	No	[21]
U-CNT-900	240	79	0.28	50	No	[22]
Co-NRCNTs	260	80	0.28	50	No	[23]
CW-CNT@N-C-Ni_3Fe	**179**	**52.8**	**0.15**	**5**	**Yes**	**This work**

References

[1] W. Bao, A. D. Pickel, Q. Zhang, Y. Chen, Y. Yao, J. Wan, K. Fu, Y. Wang, J. Dai, H. Zhu, D. Drew, M. Fuhrer, C. Dames, L. Hu, *Adv. Mater.*, **2016**, *28*, 4684.
[2] I. V. Thorat, D. E. Stephenson, N. A. Zacharias, K. Zaghib, J. N. Harb, D. R. Wheeler, *J. Power Sources,* **2009**, *188*, 592.
[3] L. Hu, H. Wu, F. La Mantia, Y. Yang, Y. Cui, *ACS Nano,* **2010**, *4*, 5843.
[4] G. Kresse, J. Hafner, *Phys. Rev. B*, **1994**, *49*, 14251.
[5] G. Kresse, D. Joubert, *Phys. Rev. B,* **1999***, 59*, 1758.
[6] B. Hammer, L. B. Hansen, J. K. Norskov, *Phys. Rev. B,* **1999**, *59*, 7413.
[7] D. Hou, W. Zhou, K. Zhou, Y. Zhou, J. Zhong, L. Yang, J. Lu, G. Li, S. Chen, *J. Mater. Chem. A*, **2015**, *3*, 15962.
[8] H. Fei, Y. Yang, Z. Peng, G. Ruan, Q. Zhong, L. Li, E. L. G. Samuel, J. M. Tour, *ACS Appl. Mater. Interfaces*, **2015**, *7*, 8083.
[9] W. Zhou, J. Zhou, Y. Zhou, J. Lu, K. Zhou, L. Yang, Z. Tang, L. Li, S. Chen, *Chem. Mater.*, **2015**, *27*, 2026.
[10] H. Fei, J. Dong, M. J. Arellano-Jiménez, G. Ye, N. Dong Kim, E. L. G. Samuel, Z. Peng, Z. Zhu, F. Qin, J. Bao, M. J. Yacaman, P. M. Ajayan, D. Chen, J. M. Tour, *Nat. Commun.*, **2015**, *6*, 8668.
[11] J. Deng, P. Ren, D. Deng, L. Yu, F. Yang, X. Bao, *Energy Environ. Sci.*, **2014**, *7*, 1919.
[12] X. Dai, Z. Li, Y. Ma, M. Liu, K. Du, H. Su, H. Zhuo, L. Yu, H. Sun, X. Zhang, *ACS Appl. Mater. Interfaces*, **2016**, *8*, 6439.
[13] S. Wu, X. Shen, G. Zhu, H. Zhou, Z. Ji, L. Ma, K. Xu, J. Yang, A. Yuan, *Carbon*, **2017**, *116*, 68.
[14] L. Lang, Y. Shi, J. Wang, F.-B. Wang, X.-H. Xia, *ACS Appl. Mater. Interfaces*, **2015**, *7*, 9098.
[15] J. Lu, T. Xiong, W. Zhou, L. Yang, Z. Tang, S. Chen, *ACS Appl. Mater. Interfaces*, **2016**, *8*, 5065.
[16] W. Zhou, Y. Zhou, L. Yang, J. Huang, Y. Ke, K. Zhou, L. Li, S. Chen, *J. Mater. Chem. A*, **2015**, *3*, 1915.
[17] J. Wang, D. Gao, G. Wang, S. Miao, H. Wu, J. Li, X. Bao, *J. Mater. Chem. A*, **2014**, *2*, 20067.
[18] Z. Xing, Q. Liu, W. Xing, A. M. Asiri, X. Sun, *ChemSusChem*, **2015**, *8*, 1850.
[19] H. Zhang, Z. Ma, J. Duan, H. Liu, G. Liu, T. Wang, K. Chang, M. Li, L. Shi, X. Meng, K. Wu, J. Ye, *ACS Nano*, **2016**, *10*, 684.
[20] Y. Yang, Z. Lun, G. Xia, F. Zheng, M. He, Q. Chen, *Energy Environ. Sci.*, **2015**, *8*, 3563.
[21] J. Deng, P. Ren, D. Deng, X. Bao, *Angew. Chem.*, **2015**, *54*, 2100.
[22] S. Gao, G. D. Li, Y. Liu, H. Chen, L. L. Feng, Y. Wang, M. Yang, D. Wang, S. Wang, X. Zou, *Nanoscale*, **2015**, *7*, 2306.
[23] X. Zou, X. Huang, A. Goswami, R. Silva, B. R. Sathe, E. Mikmeková, T. Asefa, *Angew. Chem., Int. Ed.*, **2014**, *53*, 4372.